Water Research 202 (2021) 117394

Contents lists available at ScienceDirect

Water Research

journal homepage: www.elsevier.com/locate/watres

Layered viscoelastic properties of granular biofilms

Hong-Cin Liou [a], Fabrizio Sabba [b], Ziwei Wang [a], George Wells [b], Oluwaseyi Balogun [a,b,*]

[a] Mechanical Engineering Department, Northwestern University, Evanston, IL 60208, United States
[b] Civil and Environmental Engineering Department, Northwestern University, Evanston, IL 60208, United States

ARTICLE INFO

Keywords:
Granular biofilms
Optical coherence elastography
Nondestructive viscoelastic characterization
Mechanics of granular biofilms

ABSTRACT

Granular biofilms are dense spherical complex biological systems composed mainly of multi-microbial cells, water, and extracellular polymeric substances (EPS). They facilitate efficient purification and settling of activated sludge in wastewater treatment processes. The viscoelastic properties of these complex biofilm systems are important characteristics that control their growth and dictate how they respond to hydrodynamic forces and chemical stimuli. However, the viscoelastic properties of granular biofilms are poorly understood. In this paper, we study granular biofilms' viscoelastic properties using optical coherence elastography (OCE), a nondestructive method that integrates optical coherence tomography (OCT) with elastic wave propagation. While quantitative viscoelastic characterization of granular biofilms is challenging due to their heterogeneous properties, we show that elastic waves are suitable for this purpose. First, we employ guided elastic waves in a thin section of a granular biofilm to reveal a two-layered profile for the viscoelastic properties. Next, we utilize circumferential elastic waves that propagate near the surface of a non-sectioned spherical biofilm to quantify the layered system's viscoelastic properties. To the best of our knowledge, this work is the first quantitative study that characterizes the layered viscoelastic properties of granular biofilms. The measurement approach may provide a platform to study the interplay between the viscoelastic properties and other characteristics of granular biofilms such as the complex microbial system, morphology, and oxygen distribution.

1. INTRODUCTION

Granular biofilms are microbial aggregates composed of multispecies bacterial communities and extracellular polymeric substances (EPS). Compared to conventional biofilms that colonize surfaces, granular biofilms aggregate and grow without surface attachment (Ding et al., 2015; Liu et al., 2009; Liu and Tay, 2002; Milferstedt et al., 2017). Granular biofilms have a sphere-like geometry and are recognized by different names in the literature, including granular sludge (Nancharaiah and Kiran Kumar Reddy, 2018; Wang et al., 2016), granules (Liu et al., 2009; Sarma et al., 2017), or biogranules (Liu et al., 2004; Milferstedt et al., 2017). Over the past decade, aerobic granular biofilms in sludge bioprocesses have attracted increasing interest because their operational efficiency outperforms the widely used flocculent activated sludge in wastewater processing applications for removing unwanted components (carbon, nitrogen, phosphorous, organic pollutants, etc.) (Layer et al., 2019; Milferstedt et al., 2017; Sarma et al., 2017; Wagner et al., 2015). Granular biofilms facilitate the operational efficiency in wastewater recovery due to their process intensification (decreasing process footprint and/or increasing loading rate to the process), optimal energy use, and overall cost (Liu et al., 2009; Liu and Tay, 2002; Milferstedt et al., 2017; Pronk et al., 2015; Sarma et al., 2017). Successful and sustainable implementation of granular biofilm reactors depends on the ability to predictably control biofilm growth, of which their mechanical properties are of crucial importance (Derlon et al., 2016; Liu and Tay, 2002; Nancharaiah and Kiran Kumar Reddy, 2018; Sarma et al., 2017).

Mechanical properties of granular biofilms are relevant to biofilm reactors because they control biofilms' structural stability and propensity for detachment, and in turn influence the retention of key microbial populations, the competition in biofilms, and the system functions (Aravas and Laspidou, 2008; Derlon et al., 2013; Elenter et al., 2007; Flemming and Wingender, 2010; Lackner et al., 2009; Morgenroth and Wilderer, 2000; Rittmann and Laspidou, 2003; Stoodley et al., 2002; Wells et al., 2014). The physical robustness of granular biofilms is largely attributed to the EPS, which plays a prominent role in providing cohesiveness for granulation (Flemming et al., 2016; Ras et al., 2013; Seviour et al., 2019; Zhu et al., 2012). Researchers found that EPS shares similar viscoelastic behavior with hydrogels. For example, EPS and hydrogels

* Corresponding author.
E-mail address: o-balogun@u.northwestern.edu (O. Balogun).

https://doi.org/10.1016/j.watres.2021.117394
Received 12 March 2021; Received in revised form 22 June 2021; Accepted 23 June 2021
Available online 30 June 2021
0043-1354/© 2021 Elsevier Ltd. All rights reserved.

behave as solids under small deformations and as liquids when subjected to large deformations (Lin and Wang, 2017; Ma et al., 2014; Seviour et al., 2009; Wang et al., 2016). In the small deformation regime, where elastic changes to the shape or volume of the EPS or hydrogel are less than 0.1% with respect to their equilibrium configurations, the force-displacement relationship of the materials follows the linear Hooke's law. Since hydrogels' gelation results from cross-linking of polymer molecules and the linking density controls the viscoelastic properties (Dash et al., 2013; Seidel et al., 2001; Seviour et al., 2009), it is conceivable that EPS viscoelastic properties may control the granulation of biofilms. Therefore, studying the viscoelasticity of granular biofilms may provide a more in-depth understanding of granulation processes and enhance the operational efficiency of granular biofilm reactors.

When it comes to viscoelastic characterization, rheometery is a common and versatile technique for such a purpose (Lin and Wang, 2017; Ma et al., 2014; Wang et al., 2016). However, in our previous work (Liou et al., 2019a), we reviewed several limitations of rheometery for granular biofilm characterization and proposed Optical Coherence Elastography (OCE) technique as a suitable alternative. The OCE technique relies on the measurement of propagating elastic waves in a sample and the conversion from the wave speed to the viscoelastic properties by inverse modeling. We have validated the application of OCE technique on viscoelastic characterization of soft materials in our previous papers (Liou et al., 2019a,b). When employing this technique, one thing to take note of is the depth it can probe, which is limited by the penetration depth of the OCE light source and that of the elastic wave. The former is generally less than 3 mm and the latter is in the millimeter range as circumferential waves are preferentially excited at frequencies in the kHz range. Nevertheless, since the length scale of granular biofilms also falls within the millimeter range, the limitations mentioned above are not a concern when implementing OCE measurements on them.

Specifically, this work attempts to profile the *layered* viscoelastic properties of granular biofilms using the OCE technique. The motivation for this study stems from the hypothesis that the mechanical properties of granular biofilms may vary with position due to the gradient of the oxygen concentration that may stratify the biofilm into regions with living and dead bacterial cells or form a spatial gradient of the cell population (Ding et al., 2015; Liu et al., 2009; Nancharaiah and Kiran Kumar Reddy, 2018; Sarma et al., 2017). We first probe the spatial variation of the elastic wave speed in a sectioned granular biofilm to establish the viscoelastic properties' potential layering. Next, we approximate the non-sectioned granular biofilm as a two-layered sphere with different layer properties and quantify the layers' viscoelastic properties based on OCE measurements combined with the visco-elastodynamic modeling for a layered structure. Our measurements suggest that both the shear modulus and viscosity of the granular biofilm are smaller close to the core compared to the surface, confirming the hypothesis that the viscoelastic properties are layered. One possible explanation for the core having a lower shear modulus and viscosity may be the higher biomass (i.e., bacterial cells) concentration. This assumption is verified on artificial granular biofilms where the shear modulus and viscosity are higher in pure alginate hydrogel spheres (low biomass) and lower in alginate spheres filled with activated sludge (high biomass). To the best of our knowledge, this work is the first quantitative study that reveals the layered viscoelastic properties of granular biofilms. The measurement approach and our findings reported in this paper may lay the foundation for future correlation studies of the structure, composition, and viscoelastic properties of granular biofilms.

2. MATERIALS and METHODS

2.1. Artificial graded agarose gel phantom

The layered agarose sample was created by pouring heated agarose solution in a plastic mold with the following order—1.5%, 1.25%, and 1.0% w/v of agarose concentrations. The solutions were prepared using the protocol detailed in our previous study's Supplementary Information (Liou et al., 2019b). The boiled solution (1.5%) for the first layer was poured into the mold and left to stand at ambient temperature (22 °C) for 20 min to cool down and solidify. The second layer solution (1.25%) was then poured on top of the first layer right after it was boiled in the microwave oven. The solution's temperature was still over 90 °C, so it formed a strong bond with the first layer at the interface as it cooled. After waiting for another 20 min for the second layer to cool and solidify at ambient temperature, the third layer was added by repeating the same procedure for the second layer. Note that the interfaces observed in Fig. 2a are not perpendicular to the sample surface due to the surface tension between the agarose solution and the mold wall. These angled interfaces create a gradual property change along the elastic waves' propagation path, which is a good approximation of the property variation in real biofilms.

2.2. Natural granular biofilms

The granular biofilm tested in this paper was obtained from a full-scale Aerobic Granular Sludge (AGS) Reactor (Aqua-Aerobic Systems, Inc., Rockford, IL, USA). In Section 3.2.2, the granular biofilm was cut to have a sectioned sample whose thickness is approximately 1 mm; in Section 3.2.3.2, the whole sphere-like granular biofilm was tested.

2.3. Artificial granular biofilms

Two kinds of artificial granular biofilms were made: (1) pure alginate hydrogel spheres and (2) alginate spheres filled with activated sludge. We followed the same protocol in our previous paper (Liou et al., 2019a) to prepare the alginate solution with 1.2% w/v of concentration for both kinds. The extra step to prepare the second kind of samples was adding 5 mL of concentrated activated sludge in the 45 mL of 1.2% w/v alginate solution. The activated sludge was obtained from the Terrance J. O'Brien wastewater treatment plant (Skokie, IL, USA) with the concentrations of Total Solids (TS), Total Suspended Solids (TSS), and Total Dissolved Solids (TDS), been 963.5, 355.5 and 608 mg/L, respectively, were determined following Standard Methods for the Examination of Water and Wastewater published by American Public Health Association (APHA, 1992). The 5 mL activated sludge was concentrated from 10 mL by centrifuging at 10,000 RPM for 5 min, leading to the final solids' concentration of 192.8 mg/L. Note that artificial granular biofilms are also referred as artificial biogranules in this paper.

3. RESULTS and DISCUSSION

3.1. Numerical simulation

A numerical model was developed to predict the wave speeds of circumferential elastic waves in a layered spherical structure. The model was also used for inverse analysis of OCE measurements of the elastic wave speeds in the granular biofilm samples, from which the viscoelastic properties were determined. Fig. 1a shows the configuration of the layered model. The model consists of an inner core with the radius $r = a$, an outer layer between $r = a$ and $r = b$, and an inviscid water halfspace beyond $r = b$. The water halfspace represents the native aqueous environment surrounding the biofilm. Each layer in the model is assumed to be homogeneous and isotropic. The elastic waves generated in this structure include bulk waves (longitudinal and shear waves) and circumferential interface waves. The bulk waves travel within the sample and reflect from or transmit through boundaries. The circumferential waves, on the other hand, are bound to the curved surface, and their penetration depth into the sample depends on the wavelength (or equivalently the frequency). The wave speeds of circumferential waves can be derived from the superposition of the bulk waves based on the model setup illustrated in Fig. 1a. The arrows in Fig. 1a represent the partial bulk waves (L for longitudinal; S for shear) traveling outward (+) or inward (−), and only the longitudinal wave is supported in the

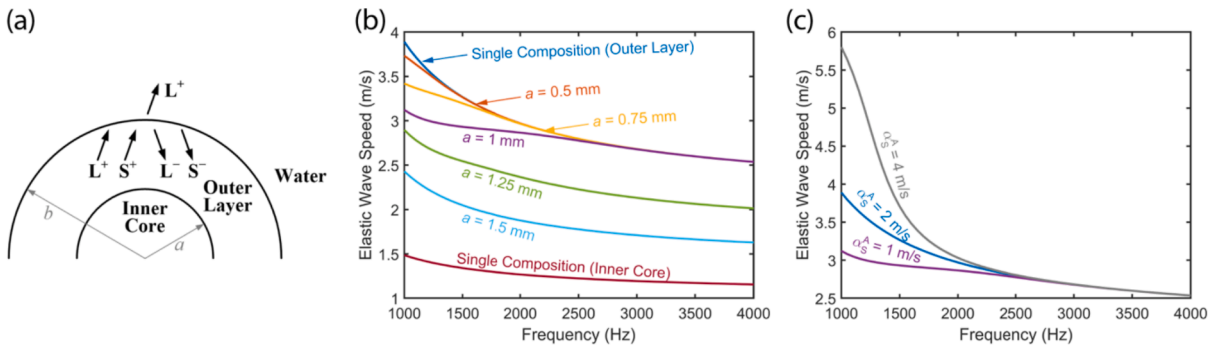

Fig. 1. (a) Two-layered cylindrical model for circumferential interface wave. (b) Comparison of dispersion curves for different inner core sizes. (c) Comparison of dispersion curves for different shear wave speeds of the inner core.

surrounding water-halfspace since it is assumed inviscid (cannot support shear motions). The water halfspace perturbs the propagation of circumferential waves at the sphere-water interface by loading the sphere surface and providing a dissipation channel for the elastic wave energy.

We remark that the circumferential elastic waves supported on the surface of a homogeneous and isotropic sphere are toroidal (Jiangong et al., 2007; Towfighi and Kundu, 2003). In the special case where the toroidal wave is monitored along the meridian that is normal to the wavefront, its propagation can be approximated by the circumferential wave traveling on the cylindrical surface with the same curvature as the meridian, which simplifies the sphere model down to a cylindrical geometry. Details of the numerical model for a homogenous and isotropic viscoelastic cylinder were published in our recent article (Liou et al., 2019a). The numerical model from that paper was extended to a two-layered viscoelastic cylinder in this work. The modeling is formulated by the following steps: (1) composing the governing elastodynamic equations using the potential functions associated with partial bulk waves, (2) expressing the components of the displacements and stress fields by the unknown amplitudes and acoustic phases of the partial waves, (3) applying boundary conditions to obtain characteristic equations, and (4) numerically solving the characteristic equations for the dispersion relation (Liou et al., 2019a, 2019b; Liu and Qu, 1998; Lowe, 1995; Rose, 1999). While the details of the governing equations, boundary conductions, and dispersion relation are provided in the Supporting Information, here we remark that the viscoelastic behavior of the biofilm is accounted for by assuming that the shear constitutive relation follows the Kevin-Voigt model as follows,

$$\overline{\mu}^{\mathrm{A}}(\omega) = \mu^{\mathrm{A}} + i\eta_{\mu}^{\mathrm{A}}\omega \tag{1}$$

$$\overline{\mu}^{\mathrm{B}}(\omega) = \mu^{\mathrm{B}} + i\eta_{\mu}^{\mathrm{B}}\omega \tag{2}$$

where $\overline{\mu}$ is the complex shear modulus, μ is the shear modulus for a purely elastic material, η_{μ} is the shear viscosity, ω is the angular frequency, and the superscripts A and B represent the inner core and the outer layer, respectively. The longitudinal wave speeds α_{L}, shear wave speeds α_{S} are defined in terms of the material density ρ and the complex first and second Lamé constants ($\overline{\lambda}$ and $\overline{\mu}$) as follows,

$$\begin{aligned}
\alpha_{\mathrm{L}}^{\mathrm{A}} &= \sqrt{\frac{\overline{\lambda} + 2\overline{\mu}^{\mathrm{A}}}{\rho}}, \\
\alpha_{\mathrm{S}}^{\mathrm{A}} &= \sqrt{\frac{\overline{\mu}^{\mathrm{A}}}{\rho}}, \\
\alpha_{\mathrm{L}}^{\mathrm{B}} &= \sqrt{\frac{\overline{\lambda} + 2\overline{\mu}^{\mathrm{B}}}{\rho}}, \\
\alpha_{\mathrm{S}}^{\mathrm{B}} &= \sqrt{\frac{\overline{\mu}^{\mathrm{B}}}{\rho}}.
\end{aligned} \tag{3}$$

For circumferential waves traveling in the two-layered cylindrical model, three important factors need to be considered: (1) the radius of curvature, (2) the ratio of the radii of the two layers, and (3) the contrast of complex Lamé constants and shear moduli (i.e., material properties) between the two layers. Since we have discussed the influence of the radius of curvature on the speed of circumferential waves in our recent publication (Liou et al., 2019a), here we focus on factors (2) and (3) to investigate how the radius ratio and the property contrast of the two layers affect the frequency-dependent speed of the circumferential wave. In the following investigations, the material properties used for the two layers are density $\rho = 1000$ kg/m^3, longitudinal wave speeds $\alpha_{\mathrm{L}}^{\mathrm{A}} = \alpha_{\mathrm{L}}^{\mathrm{B}} = 1480$ m/s, and shear wave speeds $\alpha_{\mathrm{S}}^{\mathrm{A}} = 1$ m/s, $\alpha_{\mathrm{S}}^{\mathrm{B}} = 2$ m/s. The density and longitudinal wave speed are chosen to be the same as water due to biofilms' high water content. Note that the numerical calculations in this section are restricted to pure elastic deformation with no viscous damping, so the complex wave speeds only have the real parts. In this case, the symbol α may be replaced by c to follow the conventional denotation for wave speeds.

Fig. 1b shows seven dispersion curves, and each represents the lowest order circumferential wave calculated with the numerical model for a fixed outer radius ($b = 2$ mm), fixed material properties for both layers, and different inner core radii a. All the curves show similar trends. The circumferential wave speed is higher at low frequencies and decreases monotonically as the frequency increases. The topmost and bottommost dispersion curves correspond to extreme cases of a single homogeneous composition with merely the outer layer's material properties or the inner core's, respectively. The top four dispersion curves (i.e., for $a \leq 1$ mm) converge to the same curve at high frequencies since the penetration depth of the circumferential wave—approximately equals to one wavelength (Liou et al., 2019a)—becomes smaller than the thickness of the outer layer (i.e., $b - a$). For example, at 3000 Hz, the top four curves' wave speed converges to 2.68 m/s, corresponding to a wavelength/penetration depth of 0.89 mm. At 3000 Hz and higher frequencies, the penetration depth is smaller than $b - a$; thus, the circumferential wave has limited interaction with the inner core, and the wave speed depends only on $\alpha_{\mathrm{S}}^{\mathrm{B}}$. In summary, the distribution of the seven dispersion curves from top to down show that the wave speed is sensitive to the material fraction occupied by the inner core as indicated by factor (2) listed above.

Next, we compare dispersion curves obtained from three different shear wave speeds of the inner core, $\alpha_{\mathrm{S}}^{\mathrm{A}} = 1$ m/s, 2 m/s, and 4 m/s, in Fig. 1c. The following properties: $a = 1$ mm, $b = 2$ mm, and $\alpha_{\mathrm{S}}^{\mathrm{B}} = 2$ m/s are fixed in the calculations. The three curves converge to the same curve close to 3000 Hz, where the circumferential wave's penetration depth is smaller than the outer layer thickness ($b - a$). However, below 3000 Hz, the wave speed changes appreciably with frequency for $\alpha_{\mathrm{S}}^{\mathrm{A}} = 4$ m/s. These numerical results show that the circumferential wave speed is sensitive only to the bulk shear wave speed of the outer layer at higher frequencies where the penetration depth is less than the thickness. At lower frequencies, where the penetration depth is longer than the outer

layer's thickness, the wave speed depends on the bulk shear wave speeds of both layers.

3.2. Experimental measurements

3.2.1. Spatial profiling of viscoelastic properties

This section and the following one are to test the hypothesis that granular biofilms have layered viscoelastic properties. A new measurement approach was developed to probe the spatial dependence of the elastic wave speed in graded and heterogeneous samples. We first evaluated the measurement approach in a model sample made from agarose gel with distinct boundaries that separate three regions laterally of graded agarose concentrations 1%, 1.25%, and 1.5% w/v (see Materials section). Next, in the following section, the measurement approach was applied to a sectioned thin plate-like granular biofilm.

The structural Optical Coherence Tomography (OCT), OCE, and acoustic B-scan images of the agarose sample are shown in Fig. 2a. The middle layer in the OCT image is 2 mm wide, and the widths of the other two layers are over 10 mm. The thickness and the height of the sample are 30 mm and 10 mm in the out-of-plane direction (*y*-direction) and the vertical direction (*z*-direction), respectively. The OCE image shows the full-field dynamic response of the sample induced by a 2100 Hz harmonic elastic wave. The elastic wave was actuated by a thin knife-edge that periodically impacted the sample surface. The knife-edge was connected to a piezoelectric transducer driven at 2100 Hz and was placed parallel to the *y*-direction to serve as a line source of the wave. The color contour in the OCE image represents the local vertical displacement in the sample, and the working principles of the OCT microscope to record such kind of images is detailed as follows.

The OCT microscope is basically an interferometer that is sensitive to the dynamic vertical displacement in the field of view, and thus is suitable for visualizing the shear-dominated harmonic elastic waves in the soft materials (Liou et al., 2019a). The red and blue fringes in the OCE image correspond to the optical phase difference $\Delta\phi$ (red for positive; blue for negative) measured by the OCT interferometer, which is related to the local vertical displacement u_z through the relationship $\Delta\phi = 4\pi n \Delta u_z/\lambda_0$ where n is the refractive index in the sample, λ_0 is the center wavelength of the OCT light source, and Δu_z is the displacement increment within a small time delay δt. Therefore, the fringe color is eventually related to the polarity of the displacement (red for upward; blue for downward). Note that $\Delta\phi$ varies from $-\pi$ to π radian, while Fig. 2b was plotted with saturation limits at $-\pi/2$ and $\pi/2$ radian to enhance the color contrast. When large displacement amplitudes occur, causing the $\Delta\phi$ to go over the $[-\pi, \pi]$ limit, the phase wrapping phenomenon arises and results in sign flipping of $\Delta\phi$ from blue to red or from red to blue in the center of a fringe. Since the displacement amplitudes are larger in the region close to the source (top-left in the figure), the phase wrapping is more prominent for $x \leq 4$ mm, while it is absent for $x > 4$ mm.

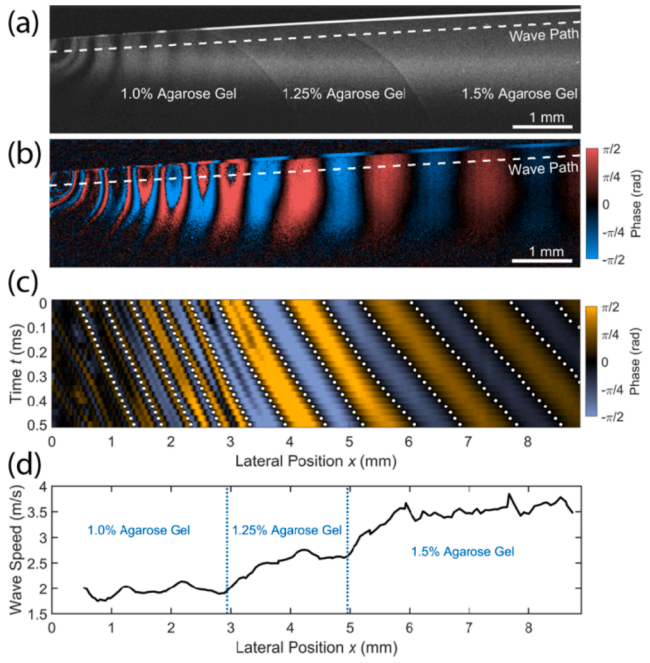

Fig. 2. Measurement of local wave speed probing on the layered agarose gel phantom. (a) OCT image showing the three layers. (b) OCE image recorded at 2.1 kHz showing the distribution of optical phase difference $\Delta\phi$. (c) Acoustic B-scan created by extracting $\Delta\phi$ from the white dashed line in (b) at different trigger delays. (d) Local wave speed estimated from the local slopes of the white dotted tracks in (c).

In total, 21 OCE images were recorded at different trigger delays t from $t = 0$ to 0.5 ms. From each OCE image, the waveform of the elastic wave was extracted along the wave path indicated by the white dashed line in Fig. 2b. The waveforms from different trigger delays were stacked row by row to create an acoustic B-scan (Fig. 2c), and the local wave speed was estimated from the local slope of the tilted color contour in Fig. 2c, as marked by the white dots in the figure. The resulting wave speed profile is shown in Fig. 2d. The two blue vertical dashed lines in Fig. 2d indicate the locations of the interfaces in the OCT image that separate the regions of different agarose concentrations. As expected, the local wave speed increases with the agarose concentration from left to right, and clear turns of the speed at $x = 3$ mm and 5 mm coincide with the interfaces where the agarose concentration changes. Furthermore, a 75% raise in speed is observed when comparing the rightmost to the leftmost regions. The resolution of this measurement approach was evaluated by finite element modeling and found to be approximately half of the elastic wavelength (see Supporting Information for more details). In addition, an animation that loops the 21 OCE images and shows the harmonic wave propagation is also available in Supporting Information.

3.2.2. Sectioned granular biofilm

In this section, the local elastic wave speed profile in a thin slice (1 mm thick) of a granular biofilm was measured. Fig. 3 shows normal microscope, OCT, OCE, and acoustic B-scan images of the sample. The central portion in the optical image (Fig. 3a) appears darker than other areas in the sample, and the radius of the dark portion is estimated qualitatively as the separation between the two vertical dashed lines. This radius of the inner core (dark region) is approximately 50% of the whole sample. Although the optical image shows the light/dark contrast, such layering distinction is not seen in the structural OCT image (Fig. 3b). Since the gray-scale intensity in the OCT image corresponds to the refractive index variation in the sample, we may conclude that the granular biofilm layering distinguished by the light/dark color contrast does not lead to a resolvable refractive index variation corresponding to an extreme property difference.

The OCE image in Fig. 3c shows the elastic wave's displacement distribution for an excitation frequency at 3200 Hz. The wave was probed along the red arrow in Fig. 3a. Since the sample slice was obtained at the equator of the biofilm sphere, we can assume that the property variation along the thickness is negligible, and changes of the local wave speed can all be attributed to the property variation along the lateral direction.

25 OCE images were recorded at different trigger delays ranging from 0 to 0.3 ms (see Supporting Information for the animated video clip). The displacement distributions extracted along the wave path (white dashed line) in Fig. 3c at all trigger delays were stacked together to produce the acoustic B-scan shown in Fig. 3d. In Fig. 3d, the signal-to-noise ratio of the OCE measurement deteriorates dramatically beyond $x = 3$ mm due to the attenuation of the elastic waves along the propagation path. The white dots in this figure mark the movement of the elastic wave with respect to time, from which the local wave speed profile

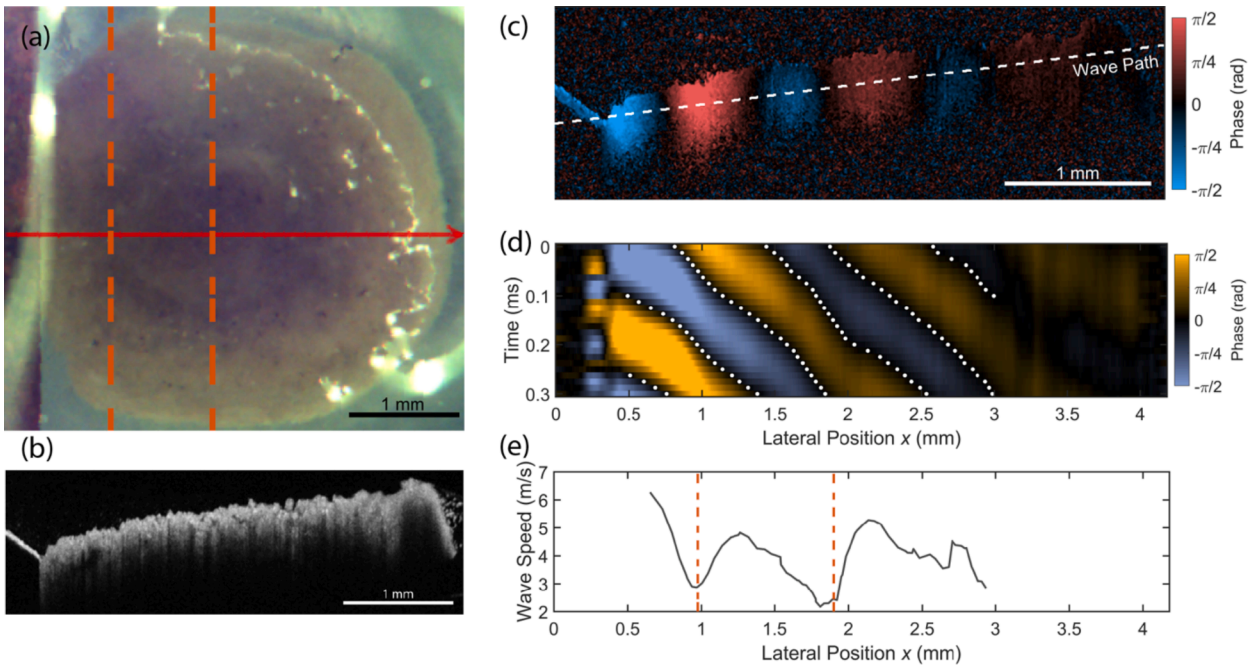

Fig. 3. Images of the granular biofilm section recorded by the OCT microscope: (a) Camera image, (b) OCT image, and (c) OCE image with wave excitation at 3200 Hz. Measurement of local wave speed probing on the granular biofilm section: (d) Acoustic B-scan created by extracting $\Delta\phi$ from the white dashed line in (c) at different trigger delays and (e) Local wave speed estimated from the local slopes of the white dotted tracks in (d).

(Fig. 3e) was estimated. Fig. 3e shows that the wave speed changes intensely along the propagation path, suggesting strong heterogeneity of the sample in terms of elastic properties. It is essential to point out that the wave speed's local variation is not due to artifacts from the OCT interferometer since the OCT image is virtually featureless. Also, during the experiment, the transducer had no translation and the sample was stationary, so the concern of motion artifacts stemming from the translation of the transducer or the sample can be dismissed. The dashed lines in Fig. 3e are at the same locations of those in Fig. 3a which indicate the center and the boundary of the sample's dark region. The wave speed profile appears to be symmetric with respect to the second dashed line (center of the biofilm sphere), and the local minima occur closely at both dashed lines as the first line marks the dark region boundary. The most important information obtained in this testing is the elastic property distinction between the light region (outer layer) and the dark region (inner core). The averaged elastic wave speed of the latter is 76% of the former (3.5 m/s to 4.57 m/s). One potential origin of the difference of the elastic wave speeds in both layers may be the spatially varying biomass (i.e., bacterial cells) concentration in the sample (Ding et al., 2015; Liu et al., 2009; Sarma et al., 2017). This assumption will be verified on artificial biogranule spheres with different biomass concentrations in the following section.

3.2.3. *Viscoelastic characterization of granular biofilms by circumferential waves*

3.2.3.1. Artificial granular biofilms. To verify the assumption stated in the previous section that a higher concentration of biomass leads to a slower elastic wave speed, we tested artificial granular biofilms made from alginate spheres with primary settling effluent sourced from a wastewater treatment plant, and compared them to the pure alginate spheres, which serve as control samples. The alginate material was chosen to mimic the viscoelastic properties of the EPS, while the primary settling effluent is a source of suspended bacteria cells. The properties of the effluent are discussed in the Materials section. We characterized the viscoelastic properties of the artificial granular biofilms based on OCE measurements of the circumferential wave speed in the samples. This measurement approach was adopted to avoid sectioning the samples. The details of the approach to quantify viscoelastic properties of pure alginate spheres can be found in a recent publication from our group (Liou et al., 2019a).

Fig. 4a and 4b show the OCT and OCE images of the alginate sphere with distributed biomass. The sample was submerged in water to mimic the native aqueous environment of real granular biofilms. The white speckles in the OCT image are the biomass aggregates. The OCE image shows the displacement pattern of a 1600 Hz harmonic circumferential wave. The white line indicates the path where the circumferential wave's displacement distribution was extracted to estimate the wavelength and the wave speed. The measurement was repeated at different frequencies to determine the frequency-dependent wave speeds as marked by the hollowed circles (for the control sample) and solid dots (for alginate with biomass) in Fig. 4c. The solid lines in Fig. 4c are the best-fits for the experimentally measured speeds obtained from theoretical calculations. Note that the theoretical calculations assumed that the samples have only one uniform composition with effective properties.

The control sample's wave speed measurements agree well with our previous report (Liou et al., 2019a), demonstrating the reliability of the sample fabrication and the repeatability of the wave speed measurement. The frequency-dependent wave speed for the control sample and artificial biogranule share similar trends. The wave speed curves have local minima between 1500 and 2500 Hz, depending on the sample composition. The clear two-group separation between the control sample and the alginate spheres with biomass indicates the distinct property difference (shear modulus and complex viscosity) between these two kinds of samples. The artificial biogranules have distinctly lower wave speeds compared to the control sample. The small variability of the wave speeds for the artificial biogranules is due to slight differences in their radii. The radii of the control sample and the biogranules are listed in Table 1. We estimated the radii by curve-fitting samples' surfaces visualized in the structural OCT images. The input viscoelastic properties and bulk shear wave speeds to achieve the best-fits for the samples are also listed in Table 1. The results suggest that the presence of biomass in the alginate spheres lowers the shear modulus and viscosity

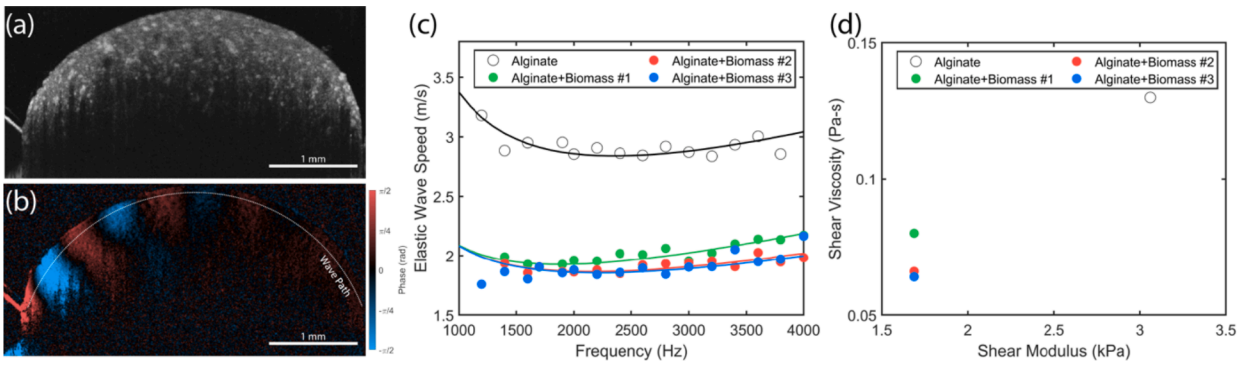

Fig. 4. (a) OCT image and (b) OCE image for the artificial alginate gel sphere with biomass. (c) Experimentally measured elastic wave speeds from spherical samples (1.2% weight-by-volume ratio of pure alginate gel in circles and Samples composed of 1.2% alginate and biomass in dots) and the best-fit dispersion curves calculated by the theoretical model (Solid lines). (d) Estimated shear moduli and shear viscosities of the samples.

of the samples. The shear modulus of the artificial biogranules is approximately 45% lower than the control, and the viscosities decrease by 46% as shown in Fig. 4d. One fortuitous outcome of the measurements is that the ratio of the bulk shear wave speeds (the artificial biogranules to the control sample) is 74.3%, close to the ratio obtained from the spatial wave speed profiling on the biofilm slice in Section 3.2.2. Based on these observations, we may confirm the assumption that the local wave speed changes observed in the sectioned biogranule may be attributed to the variation of local biomass concentrations.

3.2.3.2. Natural granular biofilm. Finally, the *layered* viscoelastic properties of the natural granular biofilm were examined by measuring the speed of circumferential waves in the sample. The granular biofilm was obtained from an aerobic granular sludge reactor at a wastewater treatment facility (See Materials section for more details). The structural OCT image of the granular biofilm are shown in Fig. 5a. The sample was submerged in a native aqueous solution from the aerobic granular sludge reactor to maintain the biofilm's natural environment. The OCT light source's penetration depth into the sample is less than 1 mm, but it is sufficient to resolve the circular outline of the biofilm surface. The radius of the sample is approximately 2.3 mm. The floating speckles near the biofilm surface are filaments. The OCT image of the biofilm does not reveal distinct structural features that may indicate the stratification or heterogeneity of the sample structural properties; rather, the morphology of the sample is uniform over the penetration depth of the OCT light source.

The OCE image in Fig. 5b shows the displacement pattern of a 3400 Hz harmonic circumferential wave along the biofilm surface. The apparent penetration depth of the displacement profile is limited by the shallow imaging depth of the OCT microscope. From the OCE image, we extracted the wavelength (1.62 mm) of the displacement pattern along the wave propagation path indicated by the white dashed line in the figure. The product of the frequency 3400 Hz and the wavelength 1.62 mm yields the wave speed 5.5 m/s.

The measured speeds of the circumferential wave at frequencies from 2600 to 5600 Hz are shown by circular dots in Fig. 5c. The wave speed of the sample is larger than the artificial biogranule. As such, longer wavelengths of the displacement pattern were recorded in the sample for the same frequencies. The green curve in Fig. 5c is the best-fit of the measured wave speeds obtained from the theoretical calculation. Note that for the calculation, as stated in the Numerical simulation section, the granular biofilm were modeled as a two-layered sphere, for which the radius of the inner core is half of the outer radius.

Furthermore, the ratio of bulk shear wave speeds (the inner core to the outer layer) was assumed to be 76%, following the result of wave speed profiling from the sectioned biofilm (Section 3.2.2). Also, given the artificial biogranules closely mimicked this 76% ratio of bulk shear wave speeds, we assumed that the viscosity ratio of the artificial biogranules (53%, the alginate spheres with biomass to the pure alginate sphere) is representative of the ratio between the inner core and the outer layer, and this ratio was used as one of the inputs for the theoretical calculation. The shear wave speed and viscosity used to obtain the best-fit are listed in Table 2. We remark that only two fitting parameters (c_S^B and η_S^B) were used in the theoretical model. From the best-fit properties, we determined the shear moduli of the outer layer and the inner core to be 8.41 kPa and 4.84 kPa, and their shear viscosities are 0.37 Pa-s and 0.20 Pa-s. The shear moduli are within the range of biofilm mechanical properties previously reported in the literature (Peterson et al., 2015).

4. CONCLUSIONS

In this paper, we studied the layered viscoelastic properties of granular biofilms based on the elastic wave speed measurements. Measurements on a thin slice of a granular biofilm from an aerobic granular sludge reactor show significant spatial variation in the speed of shear-dominated guided elastic waves. The central region of the sample has a lower wave speed compared to other parts. We hypothesized that the spatial variation of the wave speed stems from the biomass's non-uniform distribution in the granular biofilm resulting from the gradient in the sample's oxygen concentration. To support this claim, we fabricated artificial biogranules by containing primary effluent in

Table 1
Model inputs and estimated properties for artificial biogranules in Fig. 4.

Sample	Alginate	Alginate+Biomass #1	Alginate+Biomass #2	Alginate+Biomass #3
Model inputs				
Outer radius b (mm)	1.94	2.33	2.25	2.24
Density (kg/m^3)	1000	1000	1000	1000
Longitudinal wave speed (m/s)	1480	1480	1480	1480
Estimated Viscoelastic properties				
Shear wave speed (m/s)	1.75	1.3	1.3	1.3
Shear modulus (kPa)	3.06	1.69	1.69	1.69
Shear viscosity (Pa-s)	0.13	0.08	0.066	0.064

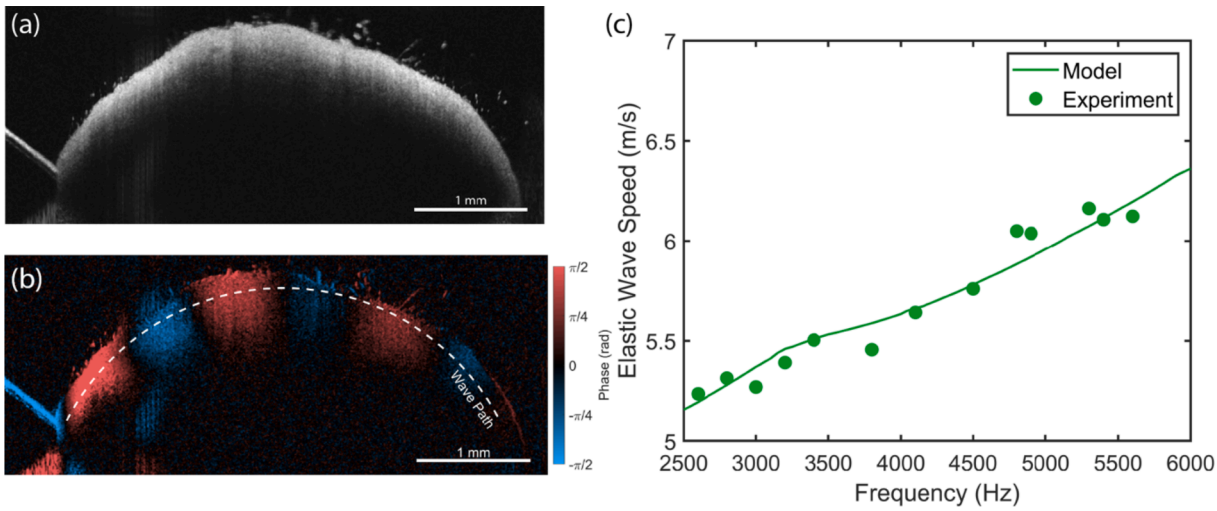

Fig. 5. (a) OCT image of the granular biofilm, (b) OCE image showing the distribution of the optical phase difference $\Delta\phi$ for circumferential interface wave at 3.4 kHz, and (c) experimentally measured elastic wave speeds and the best-fit dispersion curve calculated by the two-layered theoretical model.

Table 2
Estimated properties for the granular biofilm.

Model inputs	
Outer radius b (mm)	2.29
Inner radius a (mm)	1.15
Density (kg/m^3)	1000
Longitudinal wave speed (m/s)	1480
Estimated properties	
Shear wave speed of outer layer c_S^B (m/s)	2.9
Shear wave speed of inner layer c_S^A (m/s)	2.2
Shear viscosity of outer layer η_S^B (Pa-s)	0.37
Shear viscosity of inner layer η_S^A (Pa-s)	0.20

alginate spheres to mimic the core of the granular biofilm, while the pure alginate sample was selected to mimic the outer layer. The hypothesis is supported by our experimental observations that the viscoelastic properties of the artificial biogranules are at least 45% lower than the pure alginate sphere, confirming that biomass concentration can control granular biofilms' viscoelastic properties. Inspired by all findings above, we assumed that the non-sectioned natural granular biofilms can be modeled as two-layered spheres, leading to an inner core and an outer layer with different viscoelastic properties. We then developed a layered circumferential wave model to characterize the viscoelastic properties of the granular biofims based on the OCE measurements of the frequency-dependent circumferential wave speed and inverse analysis. The shear modulus and viscosity of the granular biofilms estimated by this approach fall within the range of reported values for biofilms.

Here we highlight two crucial points from this study. First, OCE measurement of circumferential elastic waves is a powerful tool to nondestructively characterize the viscoelasticity of biofilms with curved geometry. The circumferential waves are confined to the surface of the sample and are sensitive to the surface curvature and the viscoelastic properties. Their wavelength-dependent penetration depths potentially allow for sampling the variation of viscoelastic properties in soft materials like biofilms along the depth. Second, we quantified the spatial gradient of the viscoelastic properties in a natural granular biofilm, which not only is the first-of-its-kind report in this subject, but also supports the findings presented in the literature that granular biofilms are stratified into layers. Ongoing measurements on a statistically relevant size of granular biofilms in authors' laboratory will provide deeper insight into how consistent the heterogeneity profile is (in terms of viscoelastic properties) across samples. We will also explore local wave speed profiling with shorter wavelengths to increase the spatial resolution of the mechanical property mapping, which may lead to a more precise depiction of the layered structure in granular biofilms.

This paper lays the fundation for further studies regarding the relationships between growth conditions, morphology, and material properties of granular biofilms. By gaining more insights about the interplay between these factors, we hope to enhance the control of granular biofilms' granulation processes and ultimately facilitate their applications in wastewater treatment reactors. Finally, we remark that the measurement approach (OCE measurements of elastic waves) presented in this work is applicable not only in the biofilm field but also holds promising potential in other contexts—such as biological tissues or biomedical treatments—where the viscoelastic properties of soft materials with layered structures or complex geometries are of great interest.

Supporting information

Details about (1) the visco-elastodynamic wave model for the two-layered sphere and (2) the theoretical spatial resolution for local wave speed profiling examined by finite element simulations. (PDF)

Propagation of the elastic waves in the layered agarose sample. (mp4)

Propagation of the elastic waves in the sectioned granular biofilm. (mp4)

Declaration of Competing Interest

The authors declare that they have no known competing financial interests or personal relationships that could have appeared to influence the work reported in this paper.

Acknowledgments

We thank Aqua-Aerobic Systems, Inc. (Rockford, IL, USA) for providing granular biofilms for this work. The authors also acknowledge the National Science Foundation's support via Awards CBET-1701105 and CBET-1937290, and the seed funding from the Civil and Environmental Engineering Department at Northwestern University provided for this project.

Supporting information

Supplementary material associated with this article can be found, in the online version, at doi:10.1016/j.watres.2021.117394.

References

APHA, 1992. In: Franson, Mary Ann (Ed.), Standard methods for the examination of water and wastewater, 18th edition. American Public Health Association.

Aravas, N., Laspidou, C.S., 2008. On the calculation of the elastic modulus of a biofilm streamer. Biotechnol. Bioeng. 101, 196–200. https://doi.org/10.1002/bit.21865.

Dash, R., Foston, M., Ragauskas, A.J., 2013. Improving the mechanical and thermal properties of gelatin hydrogels cross-linked by cellulose nanowhiskers. Carbohydr. Polym. 91 https://doi.org/10.1016/j.carbpol.2012.08.080.

Derlon, N., Coufort-Saudejaud, C., Queinnec, I., Paul, E., 2013. Growth limiting conditions and denitrification govern extent and frequency of volume detachment of biofilms. Chem. Eng. J. 218, 368–375. https://doi.org/10.1016/j.cej.2012.11.061.

Derlon, N., Wagner, J., da Costa, R.H.R., Morgenroth, E., 2016. Formation of aerobic granules for the treatment of real and low-strength municipal wastewater using a sequencing batch reactor operated at constant volume. Water Res 105. https://doi.org/10.1016/j.watres.2016.09.007.

Ding, Z., Bourven, I., Guibaud, G., van Hullebusch, E.D., Panico, A., Pirozzi, F., Esposito, G., 2015. Role of extracellular polymeric substances (EPS) production in bioaggregation: application to wastewater treatment. Appl. Microbiol. Biotechnol. 99 https://doi.org/10.1007/s00253-015-6964-8.

Elenter, D., Milferstedt, K., Zhang, W., Hausner, M., Morgenroth, E., 2007. Influence of detachment on substrate removal and microbial ecology in a heterotrophic/autotrophic biofilm. Water Res 41, 4657–4671. https://doi.org/10.1016/j.watres.2007.06.050.

Flemming, H.-C., Neu, T.R., Wingender, J. (Eds.), 2016. The Perfect Slime: Microbial Extracellular Polymeric Substances (EPS). IWA Publishing.

Flemming, H.-C., Wingender, J., 2010. The biofilm matrix. Nat. Rev. Microbiol. 8, 623–633. https://doi.org/10.1038/nrmicro2415.

Jiangong, Y., Bin, W., Hongli, H., Cunfu, H., 2007. Characteristics of guided waves in anisotropic spherical curved plates. Wave Motion 44, 271–281. https://doi.org/10.1016/j.wavemoti.2006.11.002.

Lackner, S., Holmberg, M., Terada, A., Kingshott, P., Smets, B.F., 2009. Enhancing the formation and shear resistance of nitrifying biofilms on membranes by surface modification. Water Res 43, 3469–3478. https://doi.org/10.1016/j.watres.2009.05.011.

Layer, M., Adler, A., Reynaert, E., Hernandez, A., Pagni, M., Morgenroth, E., Holliger, C., Derlon, N., 2019. Organic substrate diffusibility governs microbial community composition, nutrient removal performance and kinetics of granulation of aerobic granular sludge. Water Res. X 4. https://doi.org/10.1016/j.wroa.2019.100033.

Lin, X., Wang, Y., 2017. Microstructure of anammox granules and mechanisms endowing their intensity revealed by microscopic inspection and rheometry. Water Res 120. https://doi.org/10.1016/j.watres.2017.04.053.

Liou, H.-.C., Sabba, F., Packman, A.I., Rosenthal, A., Wells, G., Balogun, O., 2019a. Towards mechanical characterization of granular biofilms by optical coherence elastography measurements of circumferential elastic waves. Soft Matter 15. https://doi.org/10.1039/C9SM00739C.

Liou, H.-.C., Sabba, F., Packman, A.I., Wells, G., Balogun, O., 2019b. Nondestructive characterization of soft materials and biofilms by measurement of guided elastic wave propagation using optical coherence elastography. Soft Matter 15. https://doi.org/10.1039/C8SM01902A.

Liu, G., Qu, J., 1998. Guided Circumferential Waves in a Circular Annulus. J. Appl. Mech. 65 https://doi.org/10.1115/1.2789071.

Liu, X.-.W., Sheng, G.-.P., Yu, H.-.Q., 2009. Physicochemical characteristics of microbial granules. Biotechnol. Adv. 27 https://doi.org/10.1016/j.biotechadv.2009.05.020.

Liu, Y.-.Q., Liu, Y., Tay, J.-.H., 2004. The effects of extracellular polymeric substances on the formation and stability of biogranules. Appl. Microbiol. Biotechnol. 65 https://doi.org/10.1007/s00253-004-1657-8.

Liu, Y., Tay, J.-.H., 2002. The essential role of hydrodynamic shear force in the formation of biofilm and granular sludge. Water Res 36. https://doi.org/10.1016/S0043-1354(01)00379-7.

Lowe, M.J.S., 1995. Matrix techniques for modeling ultrasonic waves in multilayered media. IEEE Trans. Ultrason. Ferroelectr. Freq. Control 42. https://doi.org/10.1109/58.393096.

Ma, Y.-.J., Xia, C.-.W., Yang, H.-.Y., Zeng, R.J., 2014. A rheological approach to analyze aerobic granular sludge. Water Res 50. https://doi.org/10.1016/j.watres.2013.11.049.

Milferstedt, K., Hamelin, J., Park, C., Jung, J., Hwang, Y., Cho, S.-.K., Jung, K.-.W., Kim, D.-.H., 2017. Biogranules applied in environmental engineering. Int. J. Hydrogen Energy 42. https://doi.org/10.1016/j.ijhydene.2017.07.176.

Morgenroth, E., Wilderer, P.A., 2000. Influence of detachment mechanisms on competition in biofilms. Water Res 34, 417–426. https://doi.org/10.1016/S0043-1354(99)00157-8.

Nancharaiah, Y.V., Kiran Kumar Reddy, G., 2018. Aerobic granular sludge technology: mechanisms of granulation and biotechnological applications. Bioresour. Technol. 247 https://doi.org/10.1016/j.biortech.2017.09.131.

Peterson, B.W., He, Y., Ren, Y., Zerdoum, A., Libera, M.R., Sharma, P.K., van Winkelhoff, A.-.J., Neut, D., Stoodley, P., van der Mei, H.C., Busscher, H.J., 2015. Viscoelasticity of biofilms and their recalcitrance to mechanical and chemical challenges. FEMS Microbiol. Rev. 39 https://doi.org/10.1093/femsre/fuu008.

Pronk, M., de Kreuk, M.K., de Bruin, B., Kamminga, P., Kleerebezem, R., van Loosdrecht, M.C.M., 2015. Full scale performance of the aerobic granular sludge process for sewage treatment. Water Res 84. https://doi.org/10.1016/j.watres.2015.07.011.

Ras, M., Lefebvre, D., Derlon, N., Hamelin, J., Bernet, N., Paul, E., Girbal-Neuhauser, E., 2013. Distribution and hydrophobic properties of Extracellular Polymeric Substances in biofilms in relation towards cohesion. J. Biotechnol. 165 https://doi.org/10.1016/j.jbiotec.2013.03.001.

Rittmann, B.E., Laspidou, C.S., 2003. Biofilm Detachment, in: Encyclopedia of Environmental Microbiology. John Wiley & Sons, Inc., Hoboken, NJ, USA https://doi.org/10.1002/0471263397.env012.

Rose, J.L., 1999. Ultrasonic Guided Waves in Solid Media. Cambridge University Press.

Sarma, S.J., Tay, J.H., Chu, A., 2017. Finding Knowledge Gaps in Aerobic Granulation Technology. Trends Biotechnol 35. https://doi.org/10.1016/j.tibtech.2016.07.003.

Seidel, C., Kulicke, W.-.M., Heß, C., Hartmann, B., Lechner, M.D., Lazik, W., 2001. Influence of the Cross-linking Agent on the Gel Structure of Starch Derivatives. Starch - Stärke 53. https://doi.org/10.1002/1521-379X(200107)53:7<305::AID−STAR305>3.0.CO;2-Z.

Seviour, T., Derlon, N., Dueholm, M.S., Flemming, H.-.C., Girbal-Neuhauser, E., Horn, H., Kjelleberg, S., van Loosdrecht, M.C.M., Lotti, T., Malpei, M.F., Nerenberg, R., Neu, T. R., Paul, E., Yu, H., Lin, Y., 2019. Extracellular polymeric substances of biofilms: suffering from an identity crisis. Water Res 151. https://doi.org/10.1016/j.watres.2018.11.020.

Seviour, T., Pijuan, M., Nicholson, T., Keller, J., Yuan, Z., 2009. Understanding the properties of aerobic sludge granules as hydrogels. Biotechnol. Bioeng. 102 https://doi.org/10.1002/bit.22164.

Stoodley, P., Cargo, R., Rupp, C.J., Wilson, S., Klapper, I., 2002. Biofilm material properties as related to shear-induced deformation and detachment phenomena. J. Ind. Microbiol. Biotechnol. 29, 361–367. https://doi.org/10.1038/sj.jim.7000282.

Towfighi, S., Kundu, T., 2003. Elastic wave propagation in anisotropic spherical curved plates. Int. J. Solids Struct. 40 https://doi.org/10.1016/S0020-7683(03)00278-6.

Wagner, J., Weissbrodt, D.G., Manguin, V., Ribeiro da Costa, R.H., Morgenroth, E., Derlon, N., 2015. Effect of particulate organic substrate on aerobic granulation and operating conditions of sequencing batch reactors. Water Res 85. https://doi.org/10.1016/j.watres.2015.08.030.

Wang, H.-.F., Hu, H., Yang, H.-.Y., Zeng, R.J., 2016. Characterization of anaerobic granular sludge using a rheological approach. Water Res 106. https://doi.org/10.1016/j.watres.2016.09.045.

Wells, G.F., Wu, C.H., Piceno, Y.M., Eggleston, B., Brodie, E.L., DeSantis, T.Z., Andersen, G.L., Hazen, T.C., Francis, C.A., Criddle, C.S., 2014. Microbial biogeography across a full-scale wastewater treatment plant transect: evidence for immigration between coupled processes. Appl. Microbiol. Biotechnol. 98, 4723–4736. https://doi.org/10.1007/s00253-014-5564-3.

Zhu, L., Lv, M., Dai, X., Yu, Y., Qi, H., Xu, X., 2012. Role and significance of extracellular polymeric substances on the property of aerobic granule. Bioresour. Technol. 107 https://doi.org/10.1016/j.biortech.2011.12.008.